Sufficient Utilization of $Mn^{2+}/Mn^{3+}/Mn^{4+}$ Redox in NASICON Phosphate Cathodes towards High-Energy Na-Ions Batteries

Chunliu Xu, Weibo Hua, Qinghua Zhang, Yuan Liu, Rongbin Dang, Ruijuan Xiao, Jin Wang, Zhao Chen, Feixiang Ding, Xiaodong Guo, Chao Yang, Liangrong Yang, Junmei Zhao,* and Yong-Sheng Hu**

Na superionic conductor of $Na_3MnTi(PO_4)_3$ only containing high earth-abundance elements is regarded as one of the most promising cathodes for the applicable Na-ion batteries due to its desirable cycling stability and high safety. However, the voltage hysteresis caused by Mn^{2+} ions resided in Na^+ vacancies has led to significant capacity loss associated with Mn reaction centers between 2.5–4.2 V. Herein, the sodium excess strategy based on charge compensation is applied to suppress the undesirable voltage hysteresis, thereby achieving sufficient utilization of the Mn^{2+}/Mn^{3+} and Mn^{3+}/Mn^{4+} redox couples. These findings indicate that the sodium excess $Na_{3.5}MnTi_{0.5}Ti_{0.5}(PO_4)_3$ cathode with Ti^{4+} reduction has a lowest Mn^{2+} occupation on the Na^+ vacancies in its initial composition, which can improve the kinetics properties, finally contributing to a suppressed voltage hysteresis. Based on these findings, it is further applied the sodium excess route on a Mn-richer phosphate cathode, which enables the suppressed voltage hysteresis and more reversible capacity. Consequently, this developed $Na_{3.6}Mn_{1.15}Ti_{0.85}(PO_4)_3$ cathode achieved a high energy density over 380 Wh kg^{-1} (based on active substance mass of cathode) in full-cell configurations, which is not only superior to most of the phosphate cathodes, but also delivers more application potential than the typical oxides cathodes for Na-ion batteries.

1. Introduction

Na superionic conductor (NASICON) phosphates were considered as one of the most promising cathodes for Na-ion batteries (NIBs) owing to their high safety, good structure stability, and facilitated ion transport.[1] NASICON-structured $Na_3V_2(PO_4)_3$ (NVP), as a representative case, has demonstrated the decent electrochemical performance with a long lifespan over 10 000 cycles.[2] However, limited energy density and expensive vanadium source make the raw material cost per watt hour of NVP cathode as high as 29 \$ kWh^{-1},[3] which is higher than that of the counterpart layered oxides (≈14 \$ kWh^{-1}).[4] To further increase competitiveness, extensive efforts were devoted to developing low V and V-free phosphate cathodes without sacrificing battery performance.[3,5] Among the thereby developed cathode materials, V-free $Na_3MnTi(PO_4)_3$ (NMTP) proposed by Hu et al.[5b] and investigated by Goodenough et al.,[6]

C. Xu, J. Wang, C. Yang, L. Yang, J. Zhao
CAS Key Laboratory of Green Process and Engineering
State Key Laboratory of Biochemical Engineering
Institute of Process Engineering
Chinese Academy of Sciences
Beijing 100190, P. R. China
E-mail: jmzhao@ipe.ac.cn

C. Xu, Q. Zhang, Y. Liu, R. Dang, R. Xiao, Z. Chen, F. Ding, Y.-S. Hu
Key Laboratory for Renewable Energy
Beijing Key Laboratory for New Energy Materials and Devices
Beijing National Laboratory for Condensed Matter Physics
Institute of Physics
Chinese Academy of Sciences
Beijing 100190, P. R. China
E-mail: yshu@iphy.ac.cn

C. Xu, X. Guo
School of Chemical Engineering
Sichuan University
Chengdu 610065, P. R. China
E-mail: xiaodong2009@scu.edu.cn

W. Hua
School of Chemical Engineering and Technology
Xi'an Jiaotong University
Xi'an, Shaanxi 710049, P. R. China

W. Hua
Institute of Applied Materials (IAM)
Karlsruhe Institute of Technology (KIT)
Hermann-von-Helmholtz-Platz 1 76344, Eggenstein Leopoldshafen, Germany

enables a considerable theoretical capacity of 176 mA h g^{-1} in a half cell for NIBs, through Ti^{3+}/Ti^{4+} (≈2.1 V, all versus Na/Na^+), Mn^{2+}/Mn^{3+} (≈3.5 V) and Mn^{3+}/Mn^{4+} (≈4.0 V) redox operation.[7] However, the low-voltage Ti^{3+}/Ti^{4+} is actually unavailable when matched the Na-free anode (usually hard carbon) in the practical full-cell configurations. The practically available energy density of NMTP cathode is mainly contributed by the Mn^{2+}/Mn^{3+} and Mn^{3+}/Mn^{4+} redox couples in effective voltage windows from 2.5 to 4.2 V. However, due to the existence of undesirable voltage hysteresis and the extra voltage plateaus (centered at ≈3.95 V of charge profile and ≈2.5 V discharge profile), the reversible capacities from the Mn-related redox centers in such a voltage range are usually less than two-thirds of the total discharge capacities.[6–7] Based on X-ray diffraction (XRD) refinement and electrochemical behavior, Zhang et al. suggested a possible Na^+/Mn^{2+} cation mixing in the NMTP structure and used a non-stoichiometric strategy to increase reversible capacity and voltage output.[7c] Despite the improved electrochemical performance, the structural origin and the fundamental mechanism issues behind the suppressed voltage hysteresis in NMTP system has not yet been fully studied and understood. On the other side, they proposed "Na^+/Mn^{2+} cation mixing" concept may not be accurate or rigorous because the cation mixing usually means that two ions tend to mix/exchange in both sites, such as the common Li^+/Ni^{2+} cation mixing in the nickel-based oxides for Li-ion batteries. However, considering the presence of considerable Na vacancies (6d or 18e) in the NMTP framework, the Mn^{2+} ions could easily occupy these vacancies but the Na^+ dislocation to the Mn sites is thermodynamically unfavorable due to the absence of adequate vacancies in transition metal layer. Therefore, we believe that there is only Mn^{2+} occupying Na vacancies in the NMTP system.

Herein, by employing the aberration-corrected high-angle annular dark field (HAADF)-scanning transmission electron microscopy (STEM), we revealed the occupation of Mn^{2+} on both Na1 (6b) and Na_2 (18e) vacancies in the pristine NMTP cathode for the first time, which was also confirmed by the XRD structure analyses. Such an occupation of Mn^{2+} on the Na vacancies would not only block the Na_2-Na1-Na_2 diffusing pathways to deteriorate the kinetics property, but also the dislocation of Mn^{2+} ions could cause the variation of P-O-Mn bond and the internal inductive effect, finally leading to generation of undesired voltage hysteresis and capacity loss in NMTP system. In view of this, we applied the sodium excess strategy to form Na-rich compounds $Na_{3+x}MnTi(IV)_{1-x}Ti(III)_x(PO_4)_3$ ($0 < x < 1$) by the reduction of some Ti^{4+} to Ti^{3+} ions based on charge compensation. These Na-rich cathodes provide more opportunities for Na^+ ions to occupy on the Na vacancies against Mn^{2+} during synthesis, thereby generating the suppressed voltage hysteresis. Moreover, the Ti^{3+} ions existed in the initial composition of these Na-rich phosphates could render extra capacity contribution from Ti^{3+}/Ti^{4+} reaction couple, which could be approved by the X-ray absorption spectroscopy (XAS). These redundant capacities corresponding to the low-voltage Ti^{3+}/Ti^{4+} plateau could be used for irreversible capacity consumption of HC anode during the initial cycle, without presodiation of hard carbon (HC) and addition of any sodiation reagent, which is conductive to fully utilizing high-voltage Mn^{2+}/Mn^{3+} and Mn^{3+}/Mn^{4+} redox operation in the full-cell configuration. Consequently, the Na-rich $Na_{3.5}MnTi(IV)_{0.5}Ti(III)_{0.5}(PO_4)_3$ with optimized Na content enables 356 W h kg^{-1} energy density (calculated by the mass of cathode active substance) in its full cells, far higher than that of $Na_3MnTi(PO_4)_3$ (≈280 W h kg^{-1}). To sufficiently utilizing the Mn-related redox, the sodium excess strategy was further applied to a Mn-richer phosphate system, and the optimal $Na_{3.6}Mn_{1.15}Ti_{0.85}(PO_4)_3$ cathode also displays suppressed voltage hysteresis, finally achieving a high energy density over 380 W h kg^{-1} in the full-cell configurations, which exceeds the values of the reported NMTP and well-known NVP cathodes. More impressively, owing to the well-ordered crystal structure, low raw material cost, and well-designed Na self-compensation in full cells, our $Na_{3.6}Mn_{1.15}Ti_{0.85}(PO_4)_3$ cathode shows a competitive raw material cost per energy (4 \$ kW h^{-1}), which is lower than most polyanion cathodes and metal oxides for NIBs.

2. Results and Discussion

2.1. Materials Design and Characterizations

The NASICON-type $Na_{3+x}MnTi(PO_4)_3$ ($0 < x < 1$) family was synthesized by using a typical sol-gel method. Depending on the different Na contents, these compounds were hereinafter denoted as NMTP-3.0, NMTP-3.2, NMTP-3.5, and NMTP-3.7, respectively. The structure and phase of samples were analyzed by the XRD (**Figure 1**a). Except for NMTP-3.7, all diffraction peaks of the other samples could be matched well with the calculated XRD pattern by Goodenough's early work,[6] indicative of their pure rhombohedral phase with R-3c space group. Besides, the constant shift of (300) diffraction peaks toward low angle with increase of x from 0 to 0.5 indicates the enlargement of cell volume rendered by incorporation of Na^+ (Figure 1b), which is consistent with their XRD refine results (Tables S1-S3, Supporting Information). For NMTP-3.7, substantial Na sources couldn't be fully incorporated into structure and lead to the generation of impurities (e.g., Na_3PO_4) as marked in Figure 1b. Further, the valence of transition metals was checked by the combined analysis of XAS and X-ray photoelectron spectroscopy (XPS). As shown in Figure 1c, the Mn-$L_{2,3}$ edge of NMTP-3.5 could be almost completely overlapped with the MnO spectrum for reference, revealing the bivalent Mn^{2+} features. However, the energy positions of Ti-$L_{2,3}$ edge were found to be always lower than those of the standard $BaTiO_3$ sample, implying the partial Ti^{4+} reduction after incorporation of extra alkaline Na^+ in the NMTP-3.5 (Figure 1d). The core-levels Ti 2p XPS spectra after etching indicate that the characteristic peak of NMTP-3.0 is located at ≈459 eV, which could be well assigned to tetravalent Ti^{4+} (Figure 1e). In contrast, both Ti^{3+} and Ti^{4+} signals could be searched in the XPS spectra of NMTP-3.5 (Figure 1f), which results in a Ti^{3+}/Ti^{4+} ratio of 1:1 by calculating the integral area of peaks. These results demonstrate that the incorporating excess Na^+ into NMTP system is accompanied with Ti^{4+} reduction, conforming to the charge conservation rule. Scanning electron microscopy (SEM) and transmission electron microscopy (TEM) images illustrate that nanometer-sized particles were effectively trapped in the carbon matrix (Figure S1, Supporting Information), which is favorable

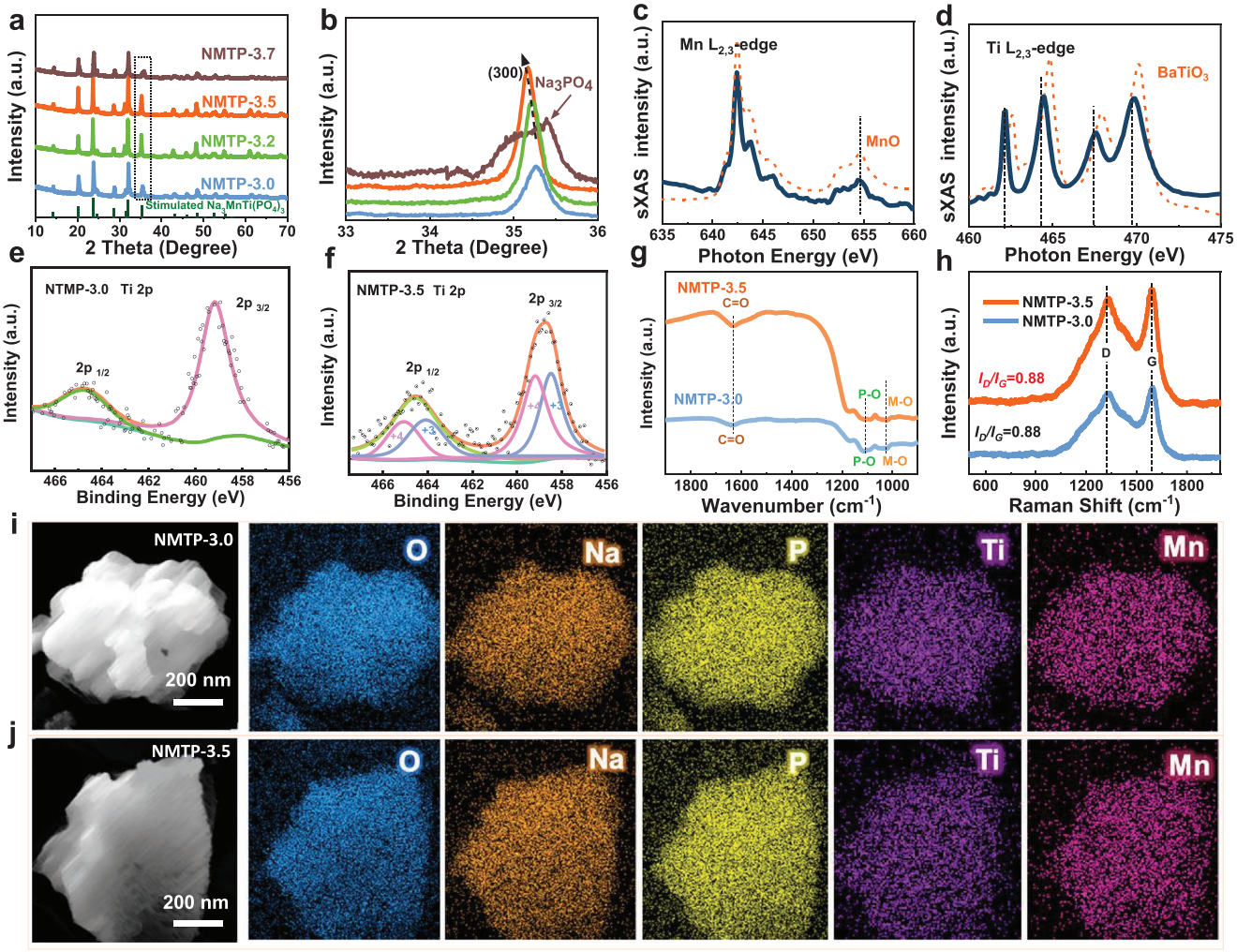

Figure 1. a) The XRD patterns of NMTP-3.0, NMTP-3.2, NMTP-3.5, and NMTP-3.7. b) The enlarged XRD patterns at the selected angles. c) Mn-$L_{2,3}$ edge and MnO as a reference and d) Ti-$L_{2,3}$ edge and $BaTiO_3$ as a reference in NMTP-3.5 XAS spectra. e) Fitted Ti 2p XPS spectra of NMTP-3.0 and f) NMTP-3.5. g) The FTIR spectra and h) Raman spectra for NMTP-3.0 and NMTP-3.5. i) The EDS mapping images of NMTP-3.0 and j) NMTP-3.5.

to improving the electronic conductivity of samples. Isothermal nitrogen desorption curve shows that NMTP-3.0 and NMTP-3.5 samples have similar specific surface area and pore size distribution (Figure S2, Supporting Information). Fourier transform infrared spectra (FTIR) confirm the presence of MO_6 (M = Ti and Mn) and PO_4 framework, as well as carbon species in both samples (Figure 1g). Raman spectra reveal the I_D/I_G ratio of ≈0.88 for two samples (Figure 1h), indicating the partial graphitization of carbon layer. Besides, the energy-dispersive X-ray spectroscopy (EDS) confirms the Na, Ti, Mn, and P elements are evenly confined in NMTP-3.0 and NMTP-3.5 particles (Figure i-j). Thermogravimetric analysis (TGA) manifests the proper carbon content of ≈8 wt.% in the as-prepared samples (Figure S3, Supporting Information).

2.2. Electrochemical Performance

The coin-type cell configurations were used to evaluate the electrochemical performance of several cathodes. The reversible capacities of 94, 101, and 112 mA h g^{-1} could be obtained for NMTP-3.0 (**Figure 2**a-b), NMTP-3.2 (Figure 2c-d), and NMTP-3.5 (Figure 2e-f) cathodes between 2.5 and 4.2 V, respectively. Besides, the low voltage plateaus centered at ≈2.2 V could be found at the beginning of the 1st charging curve for NMTP-3.2 (Figure 2c) and NMTP-3.5 (Figure 2e). The voltage plateaus were assigned to the Ti^{3+}/Ti^{4+} reaction centers due to presence of partial Ti^{3+} in their initial compositions. The capacities from Ti^{3+}/Ti^{4+} reaction for NMTP-3.2 and NMTP-3.5 are ≈11 and ≈28 mA h g^{-1}, respectively, well consistent with their theoretical Ti^{3+}content. NMTP-3.0 behaves a remarkable voltage hysteresis rooted from the large voltage gap between the extra charging plateau (≈3.95 V) and discharging plateau (≈2.5 V) (Figure S4a, Supporting Information). Obviously, such voltage hysteresis greatly lowered the capacity of the Mn^{2+}/Mn^{3+} (≈3.6 V) and Mn^{3+}/Mn^{4+} (≈4.0 V) redox couples, leading to the reversible capacity far lower than its theoretical value. In contrast, Na-rich NMTP-3.2 (Figure S4b, Supporting Information) and NMTP-3.5 (Figure S4c, Supporting Information) cathodes show suppressed voltage hysteresis and smaller electrochemical

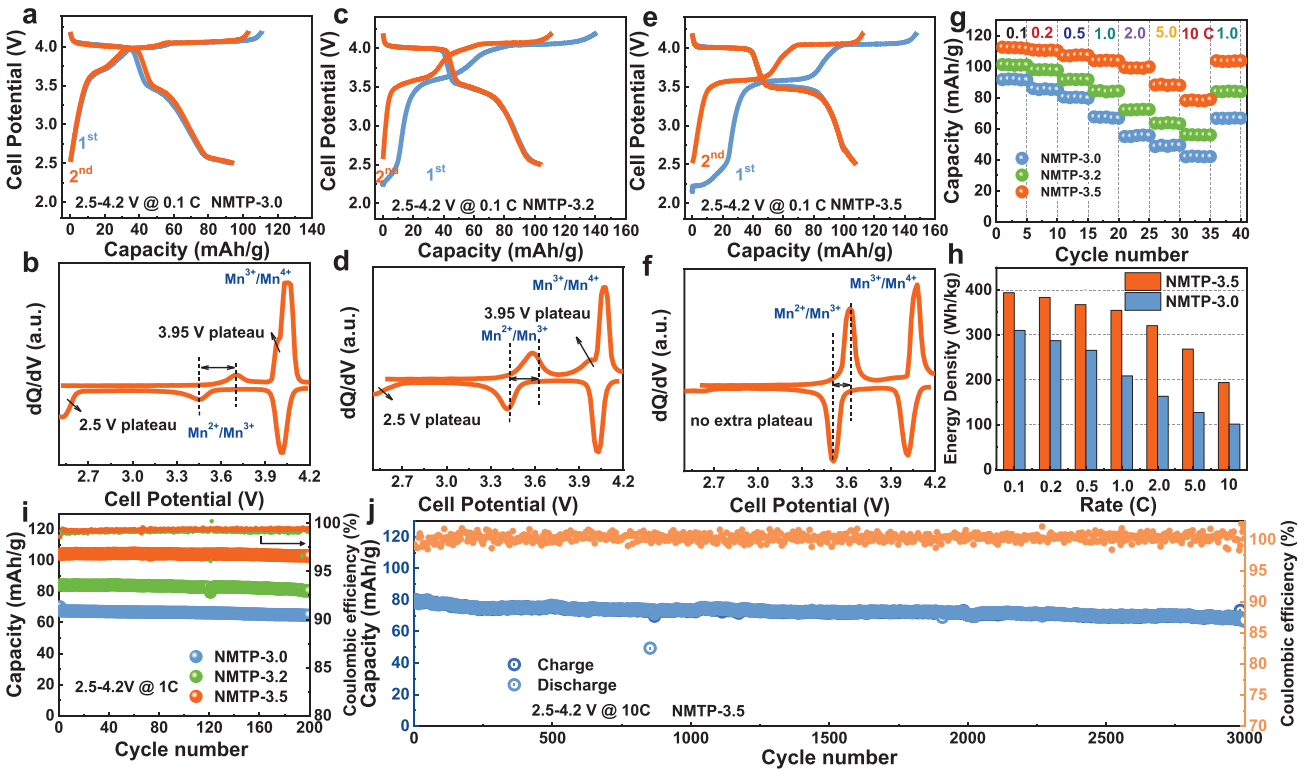

Figure 2. a) The initial charging/discharging curves of NMTP-3.0, b) NMTP-3.2, and c) NMTP-3.5 electrodes at 0.1 C. d) The rate capability comparison between several electrodes from 0.1 to 10 C in the voltage window of 2.5–4.2 V. e) The energy density of NMTP-3.0 and NMTP-3.5 cathode in the half-cell configurations based on the active substance mass. f) The cycling stability comparison between several electrodes at 1C following 200 cycles. g) The long-term cycling performance of NMTP-3.5 electrode at 10 C following 3000 cycles.

polarization. Figure 2g and Figure S5, Supporting Information, compare the rate capability of several electrodes from 0.1 to 10 C. Due to suppressed voltage hysteresis and improved electrochemical reversibility, Na-rich cathodes display better rate capability, especially for NMTP-3.5, gaining a decent capacity over 78 mA h g^{-1} at high rate of 10 C, far superior to that of NMTP-3.0 cathode (≈42 mA h g^{-1}). More importantly, owing to the absence of the undesirable voltage hysteresis, high voltage output, and sufficient capacity delivery make the energy density of NMTP-3.5 always higher than those of NMTP-3.0 cathode at various current densities (Figure 2h). Despite the excellent cycling stability for all cathodes, the low capacity (≈70 mA h g^{-1}) of NMTP-3.0 cathode hinders its further development (Figure 2i). However, Na-rich NMTP-3.5 cathode enables both high specific capacity and desirable cycling stability. For instance, NMTP-3.5 was cycled at 5 C for 500 times to achieve over 89 mA h g^{-1} reversible capacity and ≈99% capacity retention (Figure S6, Supporting Information). Further cycling at a high rate of 10 C for 3000 cycles, our NMTP-3.5 cathode still obtains a capacity of ≈72 mA h g^{-1} with retention over 90% (Figure 2j).

2.3. Atomic Structure Arrangement and Mechanism Insights

Due to the spacious framework rendered by the unique NASICON-type polyanion architecture, NMTP cathodes allow considerable Na vacancies located at Na1 (6b) and Na_2 (18e) sites.[8] Besides, considering both ionic radius and electronegativity, Mn^{2+} has a minor deviation from Na^+. These properties enable the Mn^{2+} ions tend to reside in the unoccupied Na vacancies of NMTP cathodes during synthesis. To evidence this point, the phase structure with atom occupation for NMTP-3.0 was refined by the Rietveld method. At first, we attempted to refine the structure by assuming partial Mn^{2+} ions to only occupy the Na1 (Figure S7a, Supporting Information) or Na_2 (Figure S7b, Supporting Information) vacancies alone. Despite the acceptable overall departure of R_{wp} and χ^2, the refinement was subjected to multiple iterative calculations for the final solution. In contrast, given the concurrent occupation on the Na1 or Na_2 vacancies, the stimulation of NMTP-3.0 could rapidly converged and showed the smallest difference from the experimental data (**Figure 3**a). Therefore, we refined the next XRD patterns of NMTP-3.2 (Figure S8, Supporting Information) and NMTP-3.5(Figure 3b) cathode using the same constraint except for the initial Na contents. The Rietveld refinements reveal that the Mn^{2+} occupation on the Na (both Na1 and Na_2) vacancies for NMTP-3.0 are ≈10.8% (Table S1, Supporting Information). However, the value for NMTP-3.2 (Table S2) and NMTP-3.5 (Table S3, Supporting Information) were decreased to ≈5% and ≈2%, respectively, indicative of the suppressed Mn^{2+} occupations on the Na vacancies by incorporating more Na^+ ions. Figure 3c-d display the HAADF-STEM images of NMTP-3.0 and NMTP-3.5 along [2 4 1] zone

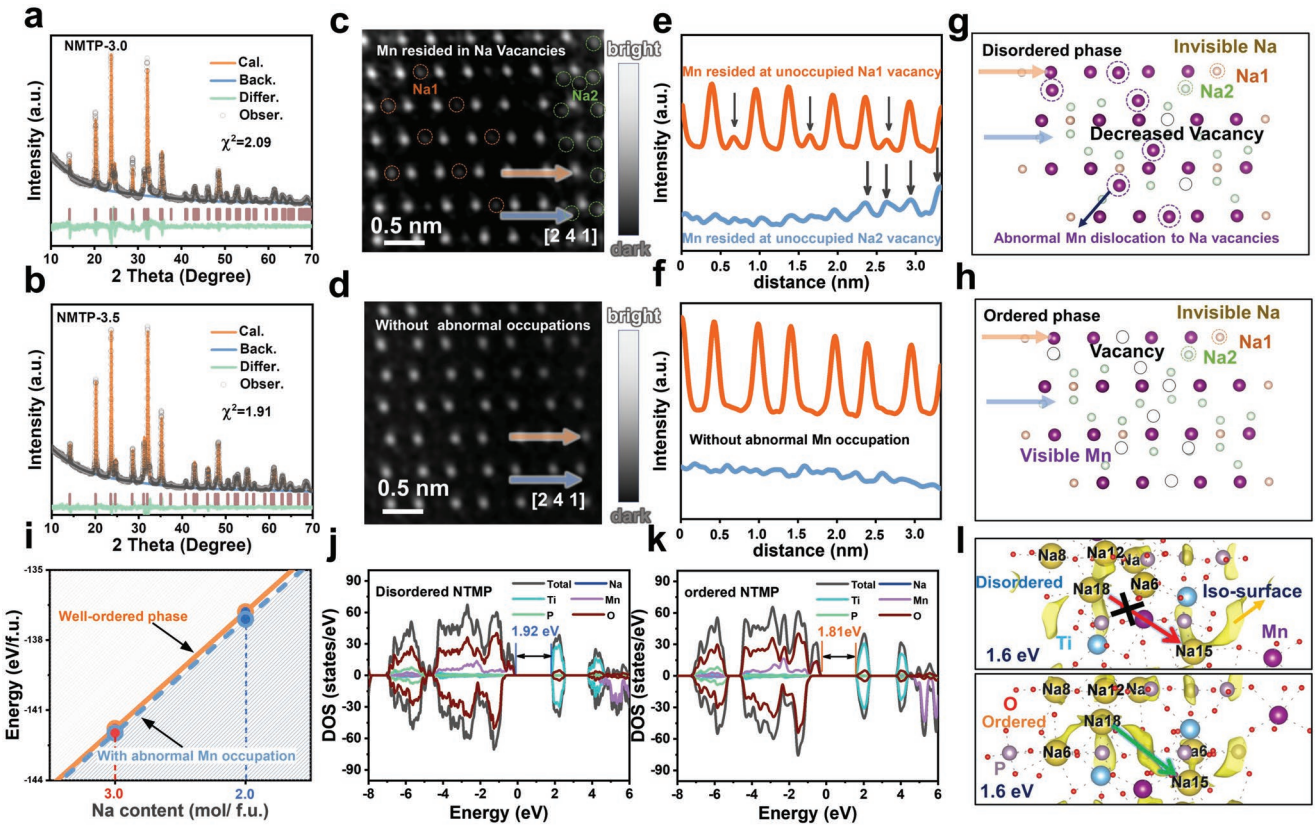

Figure 3. a,c,e,g) Rietveld refinements of the XRD patterns, HAADF-STEM images, the corresponding line profiles, and structural model illustration of NMTP-3.0 andb,d,f,h) NMTP-3.5. Both cathodes were viewed along [2 4 1] zone axis. i) The formation energy of NMTP with or without the abnormal Mn occupations per formula unites by DFT calculation. j) The total DOS and the projected element DOS of NMTP models with the abnormal Mn occupations and k) ordered structure. l) Schematic illustrations of the migration pathways represented by the yellow isosurface in two models.

axis, which enables a direct visualization of the structure and atomic arrangement.[5h,8,9] Viewing from this direction, the Na1 and Na_2 positions in a typical NASICON structure could be well distinguished as depicted in Figure S9, Supporting Information. Due to the light atomic weight, Na, O, and P elements (positions) are usually invisible in the HAADF-STEM images. Thus, the bright spots represent the heavy transition metals, i.e., Mn and Ti in our case. In good agreement with the XRD refinements, significant bright spots resided at Na sites of NMTP-3.0 structure as marked by the dotted circles, which further confirms the presence of heavy transition metals in the Na vacancies. According to the empirical formula to predict the preferred doping site (Table S4, Supporting Information), we mainly considered Mn^{2+} rather than Ti^{4+} to occupy Na vacancies. Such Mn^{2+} occupations on the Na vacancies could also be reflected and illustrated in the corresponding intensity-line plot (Figure 3e) and structural model (Figure 3g) along the given blue and orange arrows. Notably, our HAADF-STEM results present a direct proof of Mn^{2+} occupations on the Na vacancies in a NASICON structure. As a striking contrast, NMTP-3.5 shows a well-ordered rhombohedral phase without visible Mn^{2+} occupations on the Na vacancies (Figure 3d,f,h).

Furthermore, density functional theory (DFT) calculations were performed to provide more insights into the role Mn^{2+} resided in the Na vacancies on the NMTP structure. From the thermodynamics view, the total energy of NMTP with the abnormal Mn occupations on the Na vacancies (≈10%) is very close to that of the ordered NMTP phase (Figure 3i). This indicates, during the preparation of NMTP samples, symbiosis of the abnormal Mn occupations in the structure is thermodynamically favorable, well consistent with the experimental observation. Semiconductor feature of two structures was revealed by their density of states (DOS), as illustrated in Figure 3j-k. However, compared with the disordered structure with Mn^{2+} occupations on the Na vacancies, a reduced energy bandgap near the Fermi level could be observed in the ordered one, implying more favorable electronic conductivity. Besides, the Mn 3d orbitals of the ordered structure displays a richer electron density and distribution, demonstrating its higher reactivity of Mn redox center. Figure 3l compares the Na^+ migration paths shown by the yellow isosurfaces (set as 1.7 eV) in two structures. Compared with the complete isolation between "Na_{18}" and "Na_{15}" atoms for the structure with the abnormal Mn occupations (the upper in Figure 3l), the ordered NMTP reveals a broad Na^+ migration channel (the lower in Figure 3l). This result could also be experimentally demonstrated by the apparent Na-ion diffusion coefficients (D_{Na^+}) of two electrodes during (de)sodiation process (Figure S10, Supporting Information). The D_{Na^+} value of NMTP-3.0 electrode in two Mn reactive centers varies from 10^{-12} to 10^{-11} cm^2 s^{-1}, which is visibly lower than that of

NMTP-3.5 electrode (10^{-11} to 10^{-10} cm^2 s^{-1}). We believe that such sluggish Na^+ diffusion kinetics in the disordered phase should be responsible for the inferior electrochemical performance for NMTP-3.0 electrode.

Revisiting the charge/discharge curves of the as-prepared cathodes, we would have a better understanding of the electrochemical behavior. The Mn^{2+} resided in the Na vacancies in NMTP-3.0 cathode would block the Na2→Na1→Na2 diffusion pathways, which thereby deteriorates the kinetic properties and induces the significant polarization between Mn redox plateaus (Figure S11, Supporting Information). Meanwhile, due to the displacement of some Mn^{2+} (6d or 18e), partial P–O–Mn bond and the inductive effects have changed, which is confirmed by the local modeling structures of P-O-M bond between dis-/ordered $Na_3MnTi(PO_4)_3$ (Figure S12, Supporting Information). The obvious electrochemical polarization and the variation of Mn–O bond strength together contribute to the voltage hysteresis in the charge/discharge profiles for NMTP-3.0 electrode (Figure S13, Supporting Information). For NMTP-3.5 cathode, 0.5 mole Na^+ initially deintercalated from the structure during the first charging process, which is assigned to Ti^{3+}/Ti^{4+} oxidation, as illustrated in Figure S14. However, upon subsequent sodiation/desodiation between 2.5 and 4.2 V, the desodiated cathode with the nominal composition of $Na_3MnTi(PO_4)_3$ (denoted as d-NMTP-3.0) progressively experienced $Mn^{2+}/Mn^{3+}/Mn^{4+}$ redox, corresponding to a reversible two-electron reaction. The difference between d-NMTP-3.0 and NMTP-3.0 lies in a well-ordered structure for d-NMTP-3.0 but considerable abnormal Mn occupations for NMTP-3.0. Comparing their charge/discharge curves (Figure S15a, Supporting Information), we could easily find that the d-NMTP-3.0 electrode (from NMTP-3.5) always enables two clear and long voltage plateaus of Mn^{2+}/Mn^{3+} and Mn^{3+}/Mn^{4+} couples when cycled between 2.5 and 4.2 V in the subsequent cycles. As a contrast, although we changed the compositions of two electrodes by predischarge initially to the nominal compositions of $Na_4MnTi(PO_4)_3$ (Figure S15b, Supporting Information), NMTP-3.0 still shows the visible voltage hysteresis and capacity loss meanwhile NMTP-3.5 behaves two clear voltage plateaus between 2.5–4.2 V in the following cycles, which indicates the Mn^{2+} occupation fraction on the Na vacancies of two electrodes has been determined in their initial composition during the preparation process. Compared with the NMTP-3.0 case, the affluent Na^+ ions for NMTP-3.5 have more opportunities for Na^+ to occupy the Na vacancies against Mn^{2+} during synthesis, thereby generating a well-ordered structure and less voltage hysteresis.

2.4. Structural Evolution and Charge Compensation

For the purpose of elucidating the structure evolution of NMTP-3.5 electrode during (de)sodiation, we performed the in situ XRD measurements (**Figure 4**a). In the initial charging stage form the open circuit voltage (OCV, ≈2.2 V) to 2.5 V, all the diffraction peaks experienced a slight shift toward high angle, corresponding to 0.5 mol Na^+ (per f.u.) extraction for oxidation of Ti^{3+} to Ti^{4+}. Meanwhile, the NMTP-3.5 transformed into the d-NMTP-3.0 electrode. In the subsequent charging/discharging process between 2.5 and 4.2 V, the d-NMTP-3.0 electrode reversibly underwent a series of reversible visible peak changes, which includes the peak shifts, mergence/separation of peaks, and generation/disappearance of new peaks, demonstrating both solid-solution and biphasic reactions have occurred. Particularly, as described in the contour plots of the XRD (104) and (300) peaks, a single-phase reaction was involved in the low-voltage region (<3.7 V), while coexistence of two phases could be found in the high voltage range (3.7–4.2 V). On the whole, the structural evolution of NMTP-3.5 electrodes is basically consistent with the reported NMTP cathodes[7a] except for more distinct peak reflections in our case. Further, we also calculated the unit cell parameters/volume evolution of NMTP-3.5 electrode by Le Bail refinements (Figure 4b). From the pristine NMTP-3.5 to the fully charged state (4.2 V), the total volume variation ($\Delta V/V_{initial}$) is calculated to be ≈5.6% (Figure S16, Supporting Information). And such a value would further decrease to 5.1% when using the d-NMTP-3.0 as the initial state.

To unlock the charge compensation mechanism of NMTP-3.5, ex situ X-ray absorption near-edge structure (XANES) spectroscopy was performed during the first cycle. From Figure 4c, it could be found that the position of Ti K-edge first shows a significant shift towards higher energy and then maintains unchanged, indicating that Ti element has been fully oxidized to Ti^{4+} at the beginning of the charging process and stably existed as Ti^{4+} in the subsequent charging/discharging process. Figure 4d presents the XANES of Mn K-edges at the different states of charge (SOC). The Mn K-edge was found to shift rightward upon charging to 3.7 V, indicative of the valence changes from Mn^{2+} to Mn^{3+}. However, as further charging to 4.2 V, the absorption spectrum shows an obvious shift to a higher energy position, manifesting the continuous oxidation from Mn^{3+} to Mn^{4+} according to the reported Mn-based cathodes.[10] After being discharged to 2.5 V, Mn K-edges recover back to the pristine state, demonstrating an excellent reversibility. Particularly, these valence variations of elements could also be evidenced by the corresponding Ti and Mn pre-edge peak shifts (Figure 4e-f). Overall, our NMTP-3.5 electrode successively experienced the oxidation of Ti^{3+} to Ti^{4+} (≈2.2 V) and reversible redox of Mn^{2+}/Mn^{3+} (3.6 V) and Mn^{3+}/Mn^{4+} (4.1 V), consistent with the charge compensation rules. Besides, the extended X-ray absorption fine structure (EXAFS) analyses have been carried out to investigate the local environment of transition metals upon (de)sodiation. The main peaks centered at 1.4 and 3.0 Å can be observed in Figure 4g, which are assigned to the Ti–O bond and the Ti–P/O/Ti bond, respectively. With Na^+ extraction from the structure, the peak intensity of Ti–O coordination slightly increased, indicative of the elongated atom distance due to increased electro-positivity. However, there is no significant change of Ti–O bond in subsequent charging/discharging process, implying that the TiO_6 octahedral structure could be well maintained. In the case of Mn K-edge EXAFS spectra (Figure 4h), the peak of Mn-O bonds was found to split into two lower peaks upon charging to 3.7 V, which implies a positive Mn^{3+} Jahn–Teller distortion occurred in MnO_6 octahedra.[5i,10] Toward the ending of charging to 4.2 V, two peaks emerged into one peak again with an increasing intensity, suggesting the further valence transformation (Mn^{3+} to Mn^{4+}) and structural recovery. As discharged to 2.5 V, the Mn K-edge EXAFS spectrum basically recovered to its pristine state, confirming the restored MnO_6 octahedral symmetry during cycles.

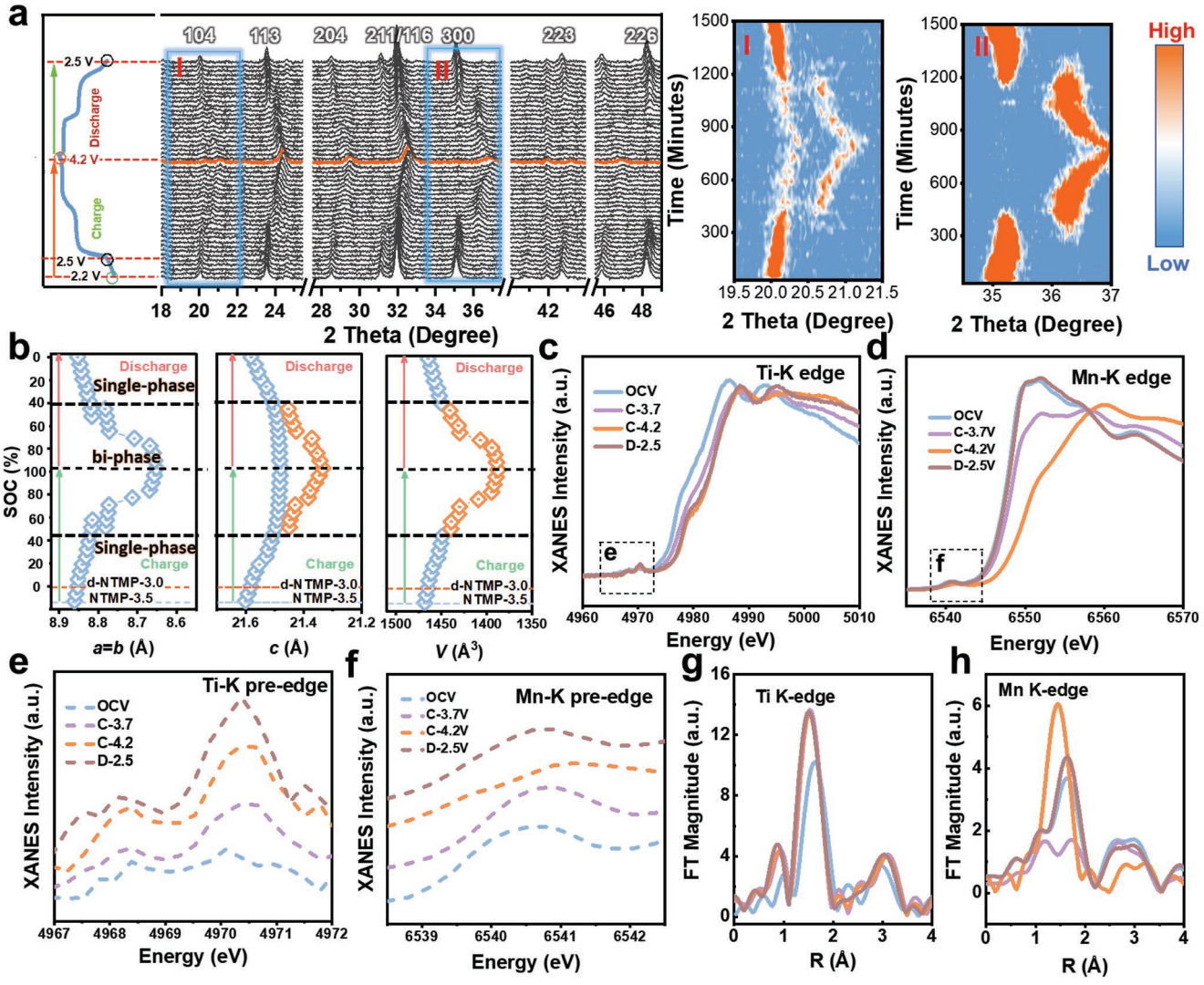

Figure 4. a) In situ XRD patterns of NMTP-3.5 electrode collected at the selected angle ranges for the first charge/discharge process. The voltage versus time curve is shown by an inset at the left. The XRD contour maps of (101) and (300) peaks are shown by an inset at the right. b) Unit cell parameters evolution during Na^+ extraction/insertion for NMTP-3.5 electrode. c) Ex situ XANES spectra at the Ti K-edge and d) Mn K-edge. e) The enlarged pre-edge region in ex situ XAFS spectra of the Ti K-edge and f) Mn K-edge. g) The corresponding ex situ EXAFS spectra of the Ti K-edge and h) Mn K-edge.

2.5. Developing Mn-Richer Cathodes and Full-Cell Performance

Further increase of Mn content in the Na-Mn-Ti-PO_4 system was always expected because more Mn reaction center would contribute to an increased theoretical energy density.[11] However, according to our findings, introduction of more Mn certainly will lead to more chance to occupied on the Na vacancies, thereby deteriorating electrochemical performance. We are encouraged that our findings have evidenced that incorporating extra Na^+ into structure is effective for suppression of the abnormal Mn occupations on the Na vacancies and the undesirable voltage hysteresis. Figure S17a, Supporting Information, compares the XRD patterns of the Mn-richer $Na_{3+2y}Mn_{1+y}Ti_{1-y}(PO_4)_3$ ($0 \le y \le 0.2$) family, where more Mn and Na ions were incorporated into structures based on charge compensation rule. It could be found that the pure rhombohedral phases were obtained in the case of $y \le 0.15$, but the diffraction peaks of $Mn_3(PO_3)_2$ impurities appeared as y further increased to 0.2. This indicates that the solution limit of Mn in the Na-Mn-Ti-PO_4 system is <1.2 mol (per f.u.). Despite incorporation more alkaline Na^+ ions into their structure, these $Na_{3+2y}Mn_{1+y}Ti_{1-y}(PO_4)_3$ ($0 \le y \le 0.2$) compounds still behave significant voltage hysteresis due to the increased structural disorder (Figure S17b, Supporting Information), on this situation, $Na_{3.3}Mn_{1.15}Ti_{0.85}(PO_4)_3$ among them delivers the highest capacities due to its high purity and increased theoretical capacity. To sufficiently activate the Mn redox couples of $Mn^{2+}/Mn^{3+}/Mn^{4+}$ for $Na_{3.3}Mn_{1.15}Ti_{0.85}(PO_4)_3$ cathode, more Na^+ ions were attempted to incorporate into its structure. The structural analysis and electrochemical behavior (Figure S18, Supporting Information) indicate that the Mn-richer cathode with a nominal composition of $Na_{3.6}Mn_{1.15}Ti_{0.85}(PO_4)_3$ (denoted as $NM_{ex}TP$-3.6) enables two distinctive voltage plateaus and suppressed voltage hysteresis, thus contributing to a reversible capacity of

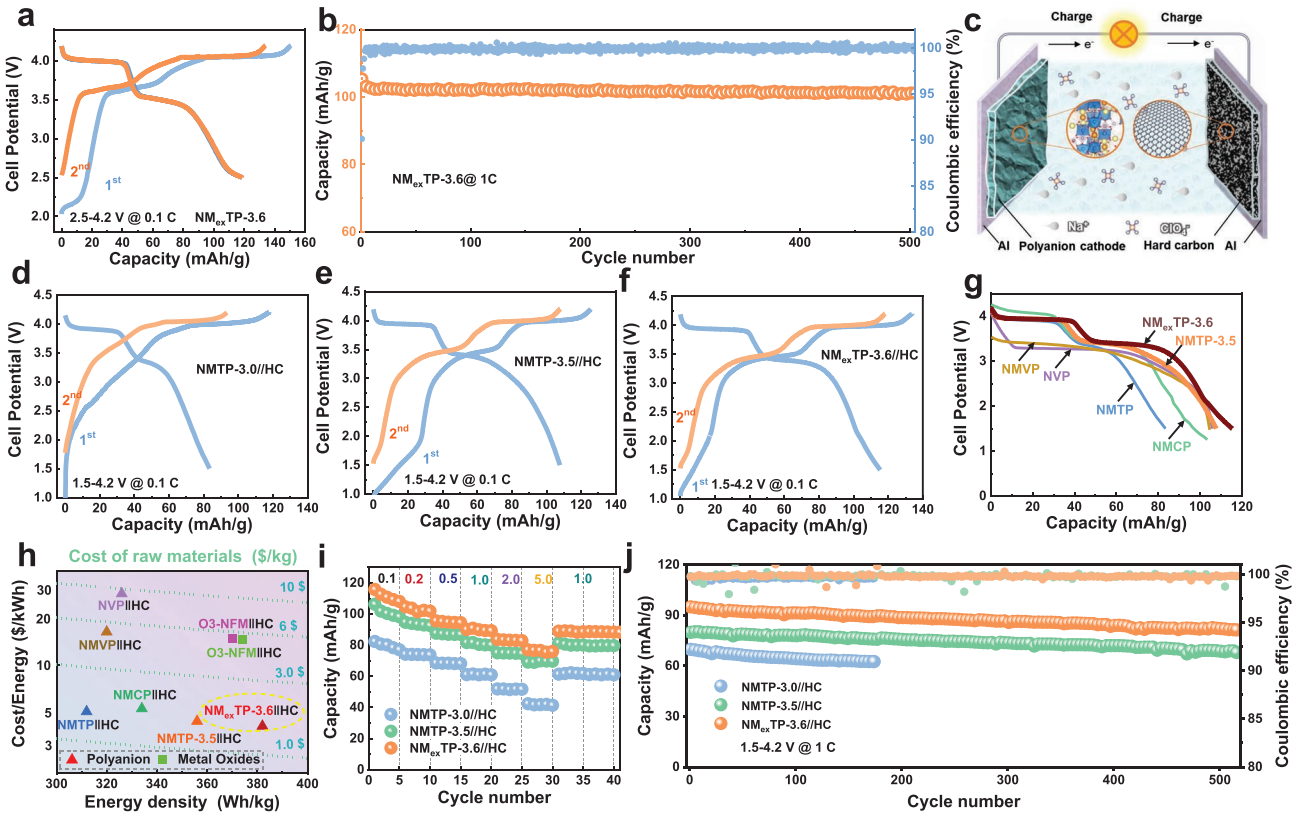

Figure 5. a) The initial two charge/discharge curves of the optimized Mn-richer $NM_{ex}TP$-3.6 electrode in the half cells. b) The cycling performance at 1 C of $NM_{ex}TP$-3.6 electrode over 500 cycles. c) Schematic illustration of our phosphates//hard carbon for Na-ion full cells. d) Initial charge/discharge curves of NMTP-3.0//HC, e) NMTP-3.5//HC, and f) $NM_{ex}TP$-3.6//HC at 0.1 C. g) Discharge voltage profiles for several typical phosphate cathodes coupled with hard carbon anodes in full cells. h) The comparison of cost per energy, energy density, and costs of raw materials between our NMTP cathodes and other phosphates as well as two representative layered oxides for NIBs. i) The rate capability and j) cycling stability of NMTP-3.0//HC, NMTP-3.5//HC, and $NM_{ex}TP$-3.6//HC full cells.

≈120 mA h g^{-1}. **Figure 5**a displays the initial two charging/discharging curves of $NM_{ex}TP$-3.6 electrode. The initial charging curve reveals ≈16.5 mA h g^{-1} capacity centered in ≈2.1 V, which could be assigned to the oxidation of Ti^{3+} to Ti^{4+}. The capacity numerical value is in basic agreement with the theoretical Ti^{3+} content in its initial composition. XRD refinements demonstrate that $NM_{ex}TP$-3.6 cathode (Figure S19a, Supporting Information) only has a total Mn^{2+} occupation fraction of ≈3.5% on the Na vacancies, which is lower than those of NMTP-3.0 (≈10%) and $NM_{ex}TP$-3.3 (≈13%, Figure S19b, Supporting Information). The rational composition design and well-ordered crystal structure make the energy density of the Mn-richer $NM_{ex}TP$-3.6 cathode reach ≈420 Wh kg^{-1} (based on cathode active substance) in half cells, far higher than that of NVP (<400 Wh kg^{-1}). Figure 5b exhibits the capacity retention cycled at 1 C within the voltage range of 2.5–4.2 V, which was calculated as 99% after 500 cycles. Such a decent electrochemical performance in half-cells impels us to further explore the practical feasibility of these Mn-rich phosphates in full-cell configurations. As graphically illustrated in Figure 5c, the hard carbon (HC) was selected as an anode to assembly the full-cell configurations. The active substance mass ratio between positive and negative electrodes was determined based on the capacity balance during the first cycle. The Na storage behavior of HC anode reveals an initial discharge capacity of ≈ 350 mA h g^{-1} with a Coulombic efficiency of over 86% (Figure S20, Supporting Information). Figure 5d records the initial charging/discharging curves of NMTP-3.0 full cells (NMTP-3.0//HC) in the voltage window of 1.5–4.2 V, which shows only 85 mA h g^{-1} reversible capacity (based on active substance mass of cathode). The capacity loss in full cells versus half cells may be caused by the irreversible Na^+ consumption for formation of solid electrolyte interface (SEI) film in HC anode surface. As a contrast, due to the redundant Na^+ (0.5 mol per f.u.) corresponding to the Ti^{3+}/Ti^{4+} reaction center could compensate the Na^+ loss during the generation of SEI layer, NMTP-3.5//HC renders a reversible capacity of ≈110 mA h g^{-1}, which is close to the value in its half-cell (Figure 5e). Such a Na-self compensation behavior has been previously demonstrated by our group in the Fe-based phosphate analogs, which is beneficial to the capacity delivery of cathode in the full-cell configurations.[12] The favorable Na-self compensation and effective suppression of voltage hysteresis make the energy density of NMTP-3.5//HC (356 Wh kg^{-1}) markedly superior to that of NMTP-3.0//HC (280 Wh kg^{-1}). More encouragingly, our developed Mn-richer $NM_{ex}TP$-3.6 full cell enables the discharge capacity of 118 mA h g^{-1} and voltage

output of 3.4 V level (Figure 5f), delivering an energy density of over 380 Wh kg^{-1}. The summary of the full-cell discharge curves in representative manganese-based phosphates and NVP cathodes (Figure 5g) clearly manifests the outstanding energy density of $NM_{ex}TP$-3.6 among the NASICON-type phosphate analogs.[5j,10,12,13] Since the cost of materials contributes to a significant proportion in the overall cell cost today, the cost of raw materials for cathode is believed to be an important consideration that cannot be ignored in the practical application.[5c] Table S5, Supporting Information, compares the cost of raw materials for the main two-type of cathodes for NIBs, i.e., polyanionic phosphates and metal oxides, which reveals NMTP-3.5 and $NM_{ex}TP$-3.6 have lower cost of raw materials, especially showing over 80% cost savings when opposed to NVP. We also observed that the V-free and Mn-based phosphates allow less cost of raw materials compared with the typical O_3-type layered oxides. To evaluate the application prospects of these cathodes more reasonably, we summarized the cost per energy ($/kWh) of various cathodes (Figure 5h), which was defined as the cost of raw materials/the energy density (based on cathode active substance in full cells). Our NMTP-3.5 and $NM_{ex}TP$-3.6 cathodes could be easily distinguished from these compounds due to their low cost per energy, i.e., 4.32 and 4.02 $/kWh, respectively, which are far lower than that of other cathodes, including recently reported polyanionic phosphates[5j,10,12,13] and two representative layered oxides.[4,14] Promising rate performance of NMTP-3.5 and $NM_{ex}TP$-3.6 full cells from 0.1 to 5 C could be observed from Figure 5i, especially for $NM_{ex}TP$-3.6 full cells, a capacity of ≈78 mA h g^{-1} was retained at a high rate of 5 C (the loading of cathode is over 15 mg cm^{-2}), far superior to that of NMTP-3.0//HC for reference (≈41 mA h g^{-1}). Cycling operation at the rate of 1 C shows both NMTP-3.5//HC and $NM_{ex}TP$-3.6//HC exhibited a stable retention over 86% after 500 cycles (Figure 5j). These observations demonstrate that the sodium excess strategy based on charge compensation enables high energy density and long cycling stability in Na–Mn–Ti–PO_4 system, shedding a light on practical application of sodium manganese titanium phosphate cathodes for NIBs in the future.

3. Conclusion

In summary, the sodium excess strategy based on charge compensation was applied to suppress the undesirable voltage hysteresis and promote the energy density of NMTP-3.0 cathode. The electrochemical behavior, XRD refinements, and HAADF-STEM observations reveal that the Mn^{2+} occupation in both Na1 and Na2 vacancies for NMTP-3.0 cathode. The block effect of Mn^{2+} resided in the Na^+ pathways and the changed inductive effect of P–Mn–O bond together led to the significant voltage hysteresis and capacity loss in the effective voltage range of 2.5–4.2 V. By a well-designed Na excess strategy based on charge compensation, the obtained NMTP-3.5 shows less structural disorder due to more opportunities for alkaline metal ions to occupy the Na vacancies against Mn^{2+} during synthesis, finally contributing to negligible voltage hysteresis and enhanced electrochemical performance. The capacity contribution from Ti^{3+}/Ti^{4+} reaction couple allows the Na-self compensation in full cells. In situ XRD and ex situ XANES demonstrate that NMTP-3.5 underwent reversible structural evolution and oxidation of Ti^{3+} to Ti^{4+} as well as reversible redox couples of $Mn^{2+}/Mn^{3+}/Mn^{4+}$. Due to sufficiently utilizing the Mn-related redox couples, the well-designed $NM_{ex}TP$-3.6//HC could achieve an increased energy density of ≈380 Wh kg^{-1} from ≈280 Wh kg^{-1} of NMTP-3.0//HC by. As a result, $NM_{ex}TP$-3.6//HC delivers a competitive cost per energy of only 4.02 $ k^{-1} W^{-1} h^{-1}, which is far lower than those of the recently reported polyanionic phosphates and two representative layered oxides, showing huge practical application potential for NIBs in the future.

Supporting Information

Supporting Information is available from the Wiley Online Library or from the author.

Acknowledgements

This work was financially supported by the following foundations: Beijing Natural Science Foundation (2222078); National Natural Science Foundation of China (52072370, 21878195, and U20A200201); Science and Technology Project of Inner Mongolia (2021GG0162); Ministry of Science and Technology of China (No. 2021YFC2901500); Excellent Member in Youth Innovation Promotion Association, Chinese Academy of Sciences (Y202014).

Conflict of Interest

The authors declare no conflict of interest.

Author Contributions

J.Z. and Y.-S.H. designed this work. C.X. prepared samples and conducted the electrochemical performance testing. C.X. wrote the original manuscripts. J.Z., X.G., and Y.-S.H. made promotion of the manuscripts and provided financial support. W.H. conducted XANES measurements. Q.Z. performed the aberration-corrected STEM shoot. R.D. performed the in situ XRD characterizations. R.X. conducted the DFT calculations. F.D. performed the s-XAS measurements. Z.C. carried out the XPS measurements. All the authors participated in the analysis of the experimental data and discussions of the results, as well as in preparing the paper.

Data Availability Statement

The data that support the findings of this study are available from the corresponding author upon reasonable request.

Keywords

Mn^{2+} occupation on Na^+ vacancies, Mn-rich phosphates, $Na_3MnTi(PO_4)_3$, Na-ion batteries, voltage hysteresis

[1] a) P. Barpanda, L. Lander, S.-i. Nishimura, A. Yamada, *Adv. Energy Mater.* **2018**, *8*, 1703055; b) S. Chen, C. Wu, L. Shen, C. Zhu, Y. Huang, K. Xi, J. Maier, Y. Yu, *Adv. Mater.* **2017**, *29*, 1700431; c) T. Jin, H. Li, K. Zhu, P. F. Wang, P. Liu, L. Jiao, *Chem. Soc. Rev.* **2020**, *49*, 2342; d) H. Li, M. Xu, Z. Zhang, Y. Lai, J. Ma, *Adv. Funct. Mater.* **2020**, *30*, 2000473; e) C. Masquelier, L. Croguennec, *Chem. Rev.* **2013**, *113*, 6552.

[2] X. Rui, W. Sun, C. Wu, Y. Yu, Q. Yan, *Adv. Mater.* **2015**, *27*, 6670.

[3] C. Xu, R. Xiao, J. Zhao, F. Ding, Y. Yang, X. Rong, X. Guo, C. Yang, H. Liu, B. Zhong, Y.-S. Hu, *ACS Energy Lett.* **2021**, *7*, 97.

[4] F. Ding, C. Zhao, D. Zhou, Q. Meng, D. Xiao, Q. Zhang, Y. Niu, Y. Li, X. Rong, Y. Lu, L. Chen, Y.-S. Hu, *Energy Storage Mater.* **2020**, *30*, 420.

[5] a) M. Chen, Q. Liu, S. W. Wang, E. Wang, X. Guo, S. L. Chou, *Adv. Energy Mater.* **2019**, *9*, 1803609. b) H. Pan, Y.-S. Hu, L. Chen, *Energy Environ. Sci.* **2013**, *6*, 2338. c) Y. Tian, G. Zeng, A. Rutt, T. Shi, H. Kim, J. Wang, J. Koettgen, Y. Sun, B. Ouyang, T. Chen, Z. Lun, Z. Rong, K. Persson, G. Ceder, *Chem. Rev.* **2021**, *121*, 1623; d) C. Xu, J. Zhao, E. Wang, X. Liu, X. Shen, X. Rong, Q. Zheng, G. Ren, N. Zhang, X. Liu, X. Guo, C. Yang, H. Liu, B. Zhong, Y. S. Hu, *Adv. Energy Mater.* **2021**, *11*, 2100729; e) W. Zhou, L. Xue, X. Lu, H. Gao, Y. Li, S. Xin, G. Fu, Z. Cui, Y. Zhu, J. B. Goodenough, *Nano Lett.* **2016**, *16*, 7836; f) J. Hou, M. Hadouchi, L. Sui, J. Liu, M. Tang, W. H. Kan, M. Avdeev, G. Zhong, Y.-K. Liao, Y.-H. Lai, Y.-H. Chu, H.-J. Lin, C.-T. Chen, Z. Hu, Y. Huang, J. Ma, *Energy Storage Mater.* **2021**, *42*, 307; g) R. Liu, G. Xu, Q. Li, S. Zheng, G. Zheng, Z. Gong, Y. Li, E. Kruskop, R. Fu, Z. Chen, K. Amine, Y. Yang, *ACS Appl. Mater. Interfaces* **2017**, *9*, 43632; h) R. Liu, S. Zheng, Y. Yuan, P. Yu, Z. Liang, W. Zhao, R. Shahbazian-Yassar, J. Ding, J. Lu, Y. Yang, *Adv. Energy Mater.* **2020**, *11*, 2003256; i) H. Gao, I. D. Seymour, S. Xin, L. Xue, G. Henkelman, J. B. Goodenough, *J. Am. Chem. Soc.* **2018**, *140*, 18192; j) T. Zhu, P. Hu, C. Cai, Z. Liu, G. Hu, Q. Kuang, L. Mai, L. Zhou, *Nano Energy* **2020**, *70*, 104548; k) M. Chen, W. Hua, J. Xiao, J. Zhang, V. W. Lau, M. Park, G. H. Lee, S. Lee, W. Wang, J. Peng, L. Fang, L. Zhou, C. K. Chang, Y. Yamauchi, S. Chou, Y. M. Kang, *J. Am. Chem. Soc.* **2021**, *143*, 18091.

[6] H. Gao, Y. Li, K. Park, J. B. Goodenough, *Chem. Mater.* **2016**, *28*, 6553.

[7] a) T. Zhu, P. Hu, X. Wang, Z. Liu, W. Luo, K. A. Owusu, W. Cao, C. Shi, J. Li, L. Zhou, L. Mai, *Adv. Energy Mater.* **2019**, *9*, 1803436; b) H. Li, M. Xu, C. Gao, W. Zhang, Z. Zhang, Y. Lai, L. Jiao, *Energy Storage Mater.* **2020**, *26*, 325; c) J. Zhang, C. Lin, Q. Xia, C. Wang, X. S. Zhao, *ACS Energy Lett.* **2021**, *6*, 2081.

[8] Z. Jian, C. Yuan, W. Han, X. Lu, L. Gu, X. Xi, Y.-S. Hu, H. Li, W. Chen, D. Chen, Y. Ikuhara, L. Chen, *Adv. Funct. Mater.* **2014**, *24*, 4265.

[9] X. Zhang, S. Guo, P. Liu, Q. Li, S. Xu, Y. Liu, K. Jiang, P. He, M. Chen, P. Wang, H. Zhou, *Adv. Energy Mater.* **2019**, *9*, 1900189.

[10] J. Zhang, Y. Liu, X. Zhao, L. He, H. Liu, Y. Song, S. Sun, Q. Li, X. Xing, J. Chen, *Adv. Mater.* **2020**, *32*, 1906348.

[11] J. Liu, K. Lin, Y. Zhao, Y. Zhou, X. Hou, X. Liu, H. Lou, K.-h. Lam, F. Chen, *J. Mater. Chem. A* **2021**, *9*, 10437.

[12] C. Xu, J. Zhao, Y. A. Wang, W. Hua, Q. fu, X. Liang, X. Rong, Q. Zhang, X. Guo, C. Yang, H. Liu, B. Zhong, Y. S. Hu, *Adv. Energy Mater.* **2022**, *12*, 2200966.

[13] G. Cui, Q. Dong, Z. Wang, X.-Z. Liao, S. Yuan, M. Jiang, Y. Shen, H. Wang, H. Che, Y.-S. He, Z.-F. Ma, *Nano Energy* **2021**, *89*, 106462.

[14] Y. Xiao, P. F. Wang, Y. X. Yin, Y. F. Zhu, Y. B. Niu, X. D. Zhang, J. Zhang, X. Yu, X. D. Guo, B. H. Zhong, Y. G. Guo, *Adv. Mater.* **2018**, *30*, 1803765.